ACS NANO
Cite This: ACS Nano XXXX, XXX, XXX−XXX
www.acsnano.org

ARTICLE

Direct Vapor−Liquid−Solid Synthesis of All-Inorganic Perovskite Nanowires for High-Performance Electronics and Optoelectronics

You Meng,[†,‡,§] Changyong Lan,[†,∥] Fangzhou Li,[†] SenPo Yip,[†,‡,§] Renjie Wei,[†] Xiaolin Kang,[†,‡,§] Xiuming Bu,[†] Ruoting Dong,[†] Heng Zhang,[†,‡,§] and Johnny C. Ho*[,†,‡,§,⊥]

[†]Department of Materials Science and Engineering, [‡]State Key Laboratory of Terahertz and Millimeter Waves, and [§]Centre for Functional Photonics, City University of Hong Kong, Kowloon, Hong Kong

[∥]School of Optoelectronic Science and Engineering, University of Electronic Science and Technology of China, Chengdu 610054, P. R. China

[⊥]Shenzhen Research Institute, City University of Hong Kong, Shenzhen 518057, P. R. China

Supporting Information

ABSTRACT: **Controlled synthesis of lead halide perovskite (LHP) nanostructures not only benefits fundamental research but also offers promise for applications. Among many synthesis techniques, although catalytic vapor−liquid−solid (VLS) growth is recognized as an effective route to achieve high-quality nanostructures, until now, there is no detailed report on VLS grown LHP nanomaterials due to the emerging challenges in perovskite synthesis. Here, we develop a direct VLS growth for single-crystalline all-inorganic lead halide perovskite (*i.e.*, $CsPbX_3$; X = Cl, Br, or I) nanowires (NWs). These NWs exhibit high-performance photodetection with the responsivity exceeding 4489 A/W and detectivity over 7.9×10^{12} Jones toward the visible light regime. Field-effect transistors (FET) based on individual $CsPbX_3$ NWs are also fabricated, where they show the superior hole mobility of up to 3.05 $cm^2/(V\ s)$, higher than other all-inorganic LHP devices. This work provides important guidelines for the further improvement of these perovskite nanostructures for utilizations.**

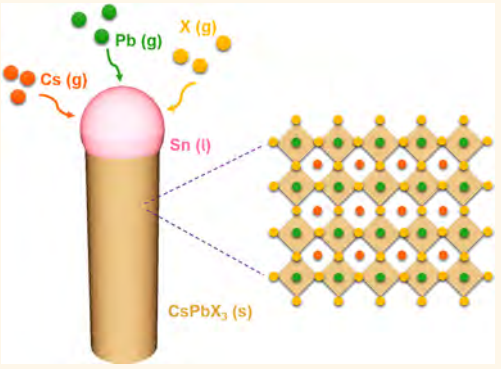

KEYWORDS: *vapor−liquid−solid, all-inorganic, perovskite, nanowire, electronic, optoelectronic*

In recent years, all-inorganic lead halide perovskites (LHPs) have been regarded as promising fundamental building blocks for next-generation electronics and optoelectronics because of their excellent material stability, high optical absorption, and long carrier diffusion length.[1−3] Since then, various methods were explored to fabricate these all-inorganic LHP materials in different morphologies, such as nanocrystals,[2,3] nanowires (NWs),[4,5] and nanoplates.[6,7] In particular, one-dimensional (1D) LHPs were demonstrated to exhibit many interesting properties, which attract wide attention to their further development for many advanced technologies.[8−11]

Generally, the vapor-phase synthesis methods are always adopted to prepare the 1D LHP nanostructures for the better crystalline quality and lower defect density as compared with the solution-phase synthesis techniques.[12−14] For instance, Chen *et al.* developed the van der Waals epitaxial growth of all-inorganic cesium lead halide ($CsPbX_3$; X = Cl, Br, or I) NW networks on mica substrates, and demonstrated their optoelectronic applications in photoluminescence wave-guiding and photodetectors.[15] Also, the guided growth of ultralong $CsPbBr_3$ NWs were realized by Shoaib *et al.* through the graphoepitaxy procedure on annealed M-plane sapphire substrates, enabling the easy fabrication of LHP NW parallel arrays.[16,17] More recently, Fan and co-workers reported the air-stable cubic-phase $CsPbI_3$ NWs synthesized inside anodic alumina membrane (AAM) templates by a chemical vapor deposition (CVD) method.[18,19] All these representative examples suggested the feasible manipulation of the crystalline phase and morphology of these obtained LHP NWs. However, all the reported $CsPbX_3$ micro-/nanowires were simply synthesized by the noncatalyzed vapor−solid (VS) growth process, instead of the catalytic vapor−liquid−solid (VLS) growth mechanism. Such a non-catalyzed VS growth process is well-known for its inferior growth of nanostructures, especially for the uncontrolled radial growth along the NW sidewalls.[20]

Received: March 27, 2019
Accepted: May 8, 2019
Published: May 8, 2019

DOI: 10.1021/acsnano.9b02379
ACS Nano XXXX, XXX, XXX−XXX

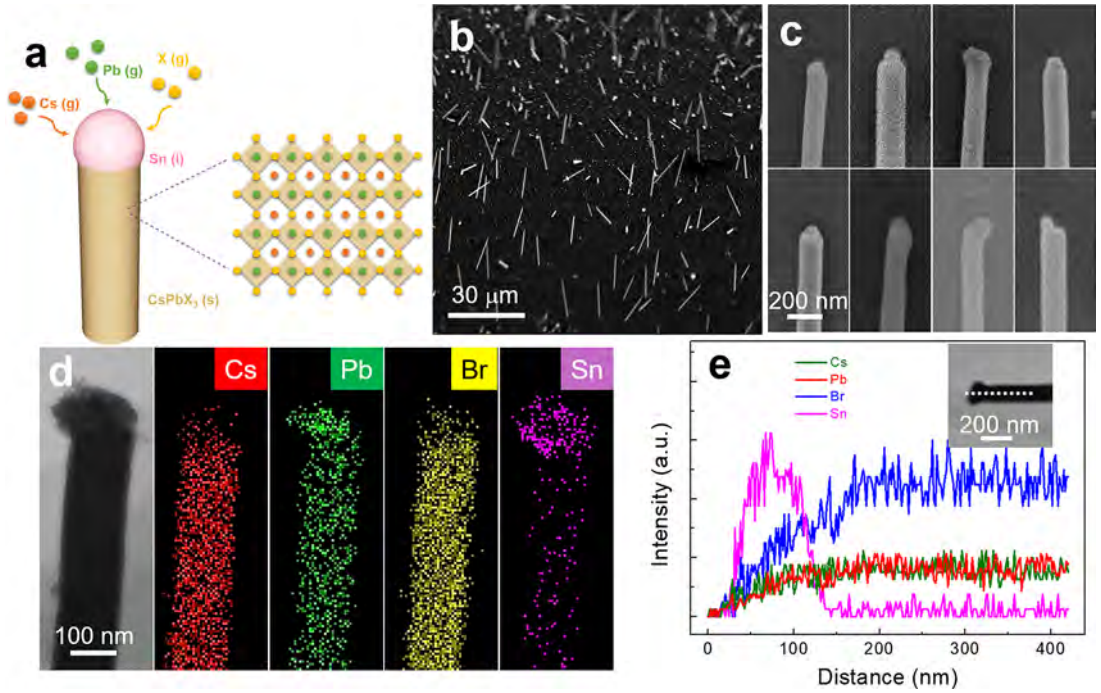

Figure 1. (a) Schematic diagram illustrating the VLS growth process of $CsPbX_3$ NW (X = Cl, Br, or I) using the Sn catalysts. (b) SEM image of the vertical $CsPbBr_3$ NWs grown on SiO_2/Si substrates. (c) Titled SEM images of different individual $CsPbBr_3$ NWs grown with the Sn catalytic seeds. (d) Typical scanning TEM image of an individual $CsPbBr_3$ NW and corresponding EDS mapping of Cs, Pb, Br, and Sn elements. (e) EDS line scan of the Sn-catalyzed $CsPbBr_3$ NW. Inset gives the corresponding TEM image with the white dashed line indicating the scanning path.

On the other hand, the catalytic VLS mechanism has been proven to be exceptionally controllable, allowing the reliable growth of various high-quality and complex low-dimensional nanostructures.[21−23] It can effectively produce highly crystalline nanomaterials with precise regulation over microstructural morphology, crystal phase, surface feature, and so on.[24−26] It also permits the modulation of chemical composition along the axial and/or radial direction of VLS-grown NWs to achieve nanoscale heterostructures.[27] These VLS-grown nanoheterojunctions have facilitated many cutting-edge applications, *e.g.*, high-mobility electron or hole gas systems, multijunction solar cells, and high-sensitivity photodetectors.[27−29] It is noted that all these fascinating features enabled by the VLS process are not quite attainable by other NW growth methodologies. To date, the VLS process has been extensively reported for the synthesis of all kinds of inorganic semiconductor nanomaterials, including group IV, III−V, and II−VI semiconductors. For LHPs, Meyers *et al.* demonstrated self-catalyzed VLS growth of lead halide (PbX_2; X = Cl, Br, or I) NWs by using liquid Pb catalysts.[30] Through a chemical conversion procedure, the as-prepared PbX_2 NWs were converted into polycrystalline methylammonium lead iodide ($MAPbI_3$) perovskite NWs with randomly oriented domains and rougher surfaces, owing to the strain induced by volume expansion during the conversion. Nevertheless, to the best of our knowledge, owing to the challenging requirement of growing ternary material systems, there is still no report on the direct VLS synthesis of low-dimensional organometallic or all-inorganic LHPs.

Here, we develop and report the VLS growth of crystalline all-inorganic $CsPbX_3$ (X = Cl, Br, or I) NWs. Specifically, large-area vertical perovskite NW arrays with a uniform diameter of ∼150 nm are successfully synthesized by using Sn catalysts. In order to understand the growth kinetics of these $CsPbX_3$ NWs, the effect of various process conditions (*i.e.*, growth pressure, growth temperature, catalyst density, and growth rate) on the NW growth are thoroughly investigated. With a relatively narrow growth process window, it is important that the grown $CsPbX_3$ NWs are defect-free and single-crystalline. When configured into photodetectors and field-effect transistors, these $CsPbX_3$ NW devices exhibit the respectable performance with high light-to-dark current ratio, large photoresponsivity, and decent mobility. All these results evidently indicate the technological potency of these VLS-grown $CsPbX_3$ NWs for high-performance electronic and optoelectronic applications.

RESULTS AND DISCUSSION

In this study, the $CsPbX_3$ (X = Cl, Br, or I) NWs were grown on SiO_2/Si substrates (270 nm thick thermal oxide) *via* a direct VLS growth process. Briefly, Sn nanoparticles with a diameter of ∼150 nm were first deposited onto the substrates as catalysts through a drop casting method. Then, a two-zone tube furnace was utilized for the NW growth. The source powder of $CsPbX_3$ was prepared by mixing CsX and PbX_2 with a molar ratio of 2:1 and was annealed at 420−460 °C for 30 min at atmosphere before being placed into a tube furnace. The prepared source powder was placed in the high-temperature zone with the temperature setting of 430−470 °C, while the substrate predeposited with Sn catalysts was put in the low-temperature zone with the temperature setting of 290−330 °C. During the NW growth, the $CsPbX_3$ powder was vaporized at elevated temperatures and carried to the low-temperature zone by argon/hydrogen gas (Ar/H_2 = 80:15) to initiate the VLS growth process. As illustrated in the schematic diagram in Figure 1a, the Sn catalyst would exist in the liquid state due to its low melting point of 232 °C and get supersaturated through the addition of vapor-phase precursors, *i.e.*, Cs, Pb, and X (X = Cl, Br, or I), inducing the growth of $CsPbX_3$ NWs at the liquid−solid interface.[31] By maintaining these conditions for a duration of

DOI: 10.1021/acsnano.9b02379
ACS Nano XXXX, XXX, XXX−XXX

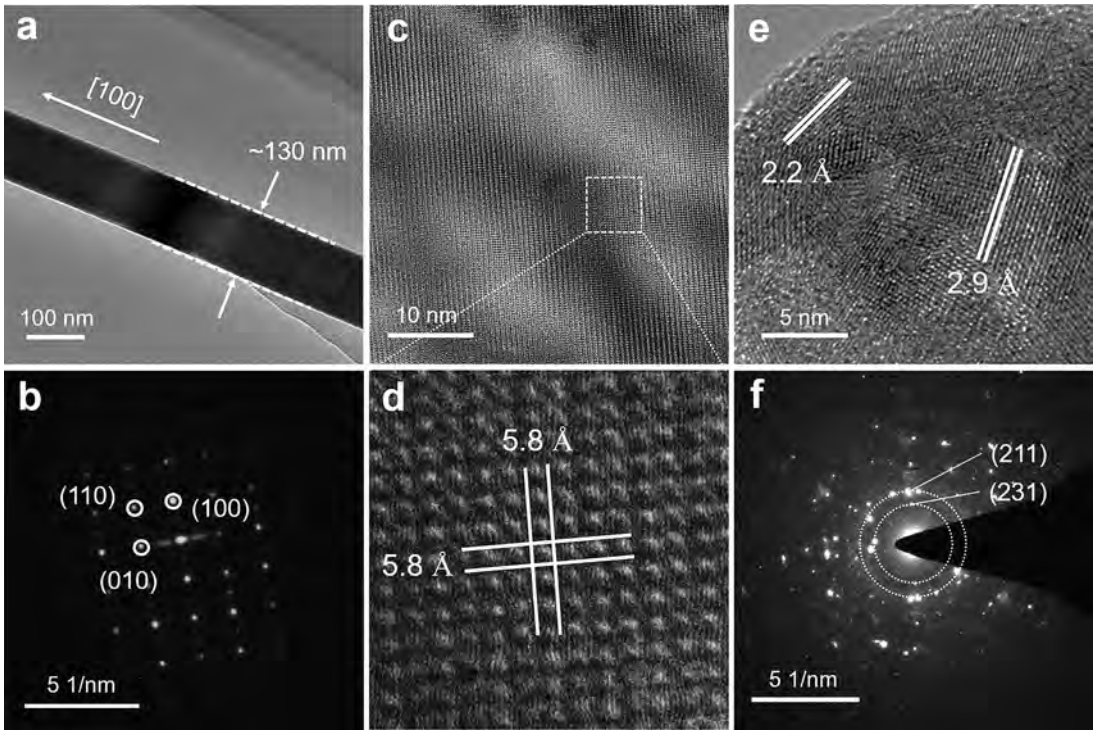

Figure 2. (a) TEM image and (b) corresponding SAED pattern of a typical VLS-grown $CsPbBr_3$ NW. (c, d) HRTEM images of the $CsPbBr_3$ NW body. (e) HRTEM image and (f) corresponding SAED pattern of the VLS-grown $CsPbBr_3$ NW tip.

60−300 min, there was a good yield of NWs growing on the substrate (Figure S1). The details of the NW growth are provided in the Methods section.

Afterward, the morphology of grown $CsPbBr_3$ NWs was carefully evaluated by scanning electron microscopy (SEM). It is clear that the vertical growth of $CsPbBr_3$ NWs is observed on the substrate (Figure 1b), whereas distinctive spherical-like catalytic seeds are witnessed in the tip region of individual NWs (Figure 1c), designating the VLS growth process here. When the control experiments are performed without using any Sn catalyst, no NWs are grown on the substrate under the same process conditions, further confirming the necessity of predeposited Sn catalysts to yield the NW growth (Figure S2). This also shows the potential of defining the locations of the nanowire growth *via* simply manipulating the catalyst position. Notably, based on the detailed energy-dispersive X-ray spectroscopy (EDS) mapping (Figure 1d), the catalytic tip of the $CsPbBr_3$ NW is composed mainly of Sn and Pb, while the NW body is made up of Cs, Pb, and Br with a uniform distribution. This high Pb content of the tip is anticipated due to the relatively low Sn−Pb eutectic melting temperature of 183 °C for the efficient supersaturation process of the catalyst tip.[30] In contrast, the low equilibrium solubility of Cs and Br in liquid Sn would lead to the low elemental content of Cs and Br in the tip during NW growth. In this case, the NWs are confirmed to grow *via* the VLS mechanism through supersaturation of Cs and Br in a liquid Sn−Pb catalyst. The composition quantification is also performed along the axial direction of the NW (Figure 1e), which further verifies the uniform elemental distribution of Cs, Pb, and Br, having a composition ratio of 1:1:3 and being in agreement with the stoichiometric ratio of $CsPbBr_3$ (Figure S3). It should also be noted that the NW body composes a trace amount of Sn, which is below the detection limit of EDS (Figure S3). Chemical doping of metal (*e.g.*, Mn^{2+}, Zn^{2+}, Sn^{2+}, Sb^{3+}, and Bi^{3+}) into LHPs has been proven to be a relatively effective approach to solve the issues of instability and toxicity, while providing additional tunable physical and chemical properties.[32,33] In a recent work, LHPs incorporating the lighter-element Sn would lead to an upshift in the longitudinal optical (LO) phonon frequencies, which is advantageous for the high charge-carrier mobility.[34] The effect of these Sn residuals on the NW properties are still in the process of thorough investigation. In any case, similar VLS growth processes are also demonstrated with $CsPbCl_3$ and $CsPbI_3$ NWs, where the distinctive catalytic tips are clearly observed, indicating the NWs grown with the VLS mechanism here (Figures S4 and S5). In principle, perovskite NWs can also be grown *via* the formation of PbX_2 NWs followed by the *in situ* chemical conversion into perovskites. Characteristically, these converted perovskite NWs exhibit the polycrystallinity with randomly oriented domains and rougher surfaces, owing to the strain induced by volume expansion during the chemical conversion.[12,30,35] As shown in the TEM images in Figures 2, 4, S4, and S5, single-crystalline $CsPbX_3$ NWs with smooth surfaces are obtained by using our direct VLS growth process; therefore, it can also probably rule out the possibility of our perovskite NWs grown *via* the *in situ* chemical conversion from PbX_2 to perovskites.

At the same time, the crystallinity of VLS-grown $CsPbBr_3$ NWs was also evaluated with transmission electron microscopy (TEM) and selected-area electron diffraction (SAED) in detail (Figure 2a and 2b). According to the SAED patterns collected from multiple NWs, almost all of the NWs are grown with an orientation of [100]. As supported by the density functional theory (DFT) calculations, since the surface free energy of (100) planes of $CsPbBr_3$ is lower than that of other planes, $CsPbBr_3$ NWs are expected to grow along the [100] direction.[36,37] When the SAED patterns are collected along the NW axial direction, the same growth direction of [100] is

DOI: 10.1021/acsnano.9b02379
ACS Nano XXXX, XXX, XXX−XXX

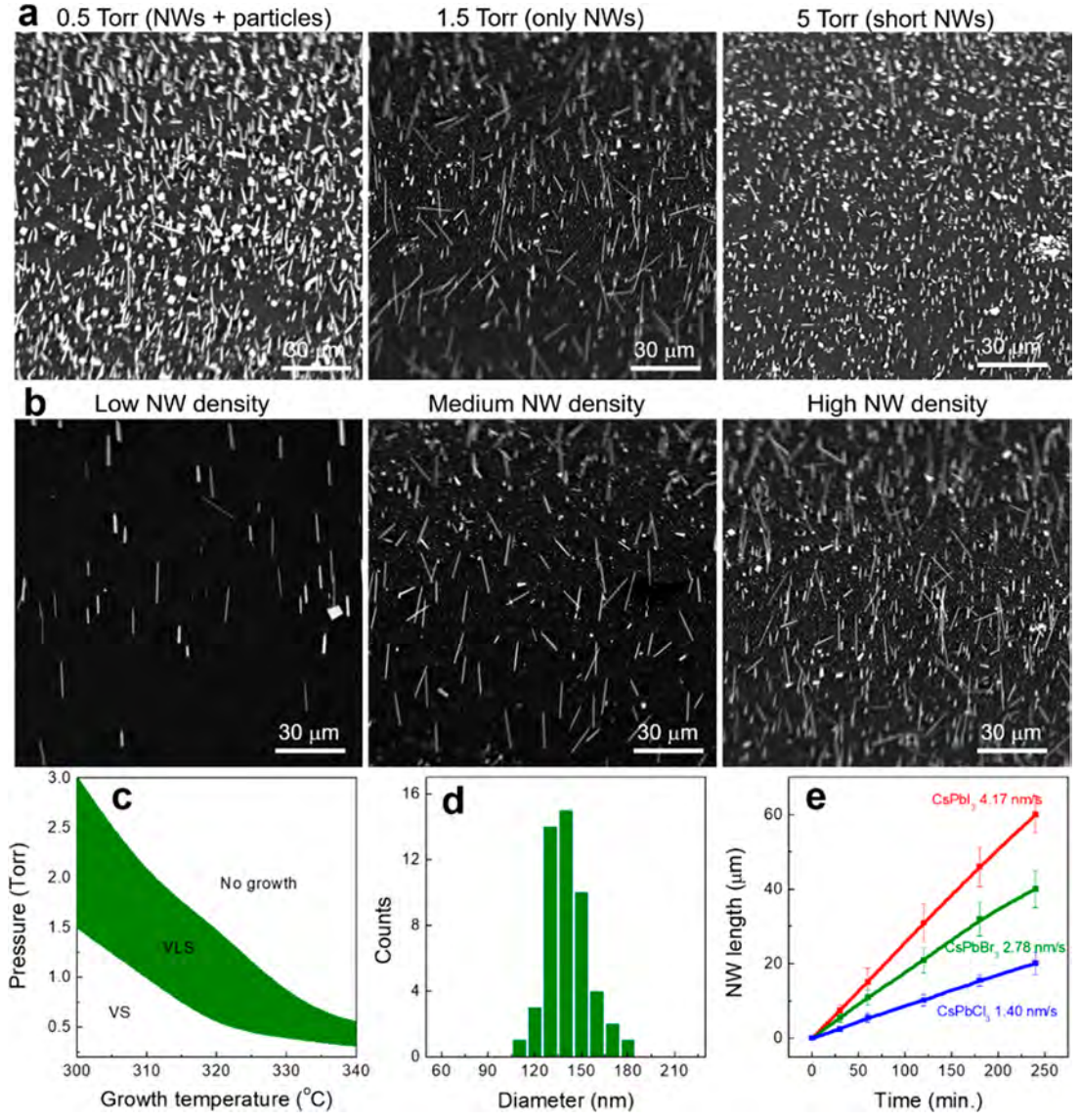

Figure 3. Titled SEM images of VLS-grown $CsPbBr_3$ NWs with (a) different growth pressure and (b) different NW density. (c) Temperature-dependent and pressure-dependent VLS-growth window for $CsPbBr_3$ NWs. (d) Diameter statistical distribution of the as-grown $CsPbBr_3$ NWs. (e) Length of $CsPbX_3$ (X = Cl, Br, or I) NWs as a function of the growth time.

confirmed, suggesting the excellent crystallinity without any phase inversion defects along the entire length of the NW. This is also consistent with the high-resolution TEM (HRTEM) result that the continuous lattice fringes are visibly observed across the NW body (Figure 2c), providing additional evidence for the crystallinity and growth characteristics of NWs. Explicitly, Figure 2d exhibits the clear lattice fringes with a spacing of 5.8 Å, which corresponds to the lattice spacing of {100} planes of the cubic $CsPbBr_3$ crystal. This cubic phase is also in perfect agreement with the XRD result, which will be discussed later. All these results can further confirm the VLS-grown $CsPbBr_3$ NW having a defect-free single-crystalline characteristic. Importantly, as shown in Figure S6, the XRD patterns and normalized PL spectra of $CsPbBr_3$ NWs illustrate the existence of diffraction peaks from their cubic phase as well as a sharp emission characteristic peak at 539 nm, even after 60 days of storage in ambient conditions. These observations can evidently indicate the excellent material stability of $CsPbBr_3$ NWs fabricated by the VLS growth process.

Meanwhile, we try to evaluate the crystallinity of the catalytic seed existing in the NW tip. Evidently, the polycrystalline nature with obvious crystal boundaries are observed in the HRTEM image (Figure 2e), while the corresponding diffraction spots appear in a complicated manner in the SAED pattern (Figure 2f). These polycrystalline seeds are quite commonly observed for the VLS growth of high-quality semiconductor NWs.[38] Because the melting point of Sn (232 °C) or Sn−Pb (183 °C) is lower than the growth temperature (310 °C) of $CsPbBr_3$ NWs, it is anticipated that the molten catalytic seeds would become solidified in a polycrystalline phase after termination. The marked interplanar spacings in HRTEM image (Figure 2e) are measured to be 2.2 and 2.9 Å, which are close to the (231) interplanar spacing of 2.208 Å and (211) interplanar spacing of 2.924 Å for $PbBr_2$ (JCPDS No. 31-0679). The corresponding diffraction spots of (231) and (211) planes are also found in the SAED pattern (Figure 2f), further indicating the possible formation of $PbBr_2$. From the viewpoint of a recrystallization process, the existence of $PbBr_2$ is probably due to the abundant

DOI: 10.1021/acsnano.9b02379
ACS Nano XXXX, XXX, XXX−XXX

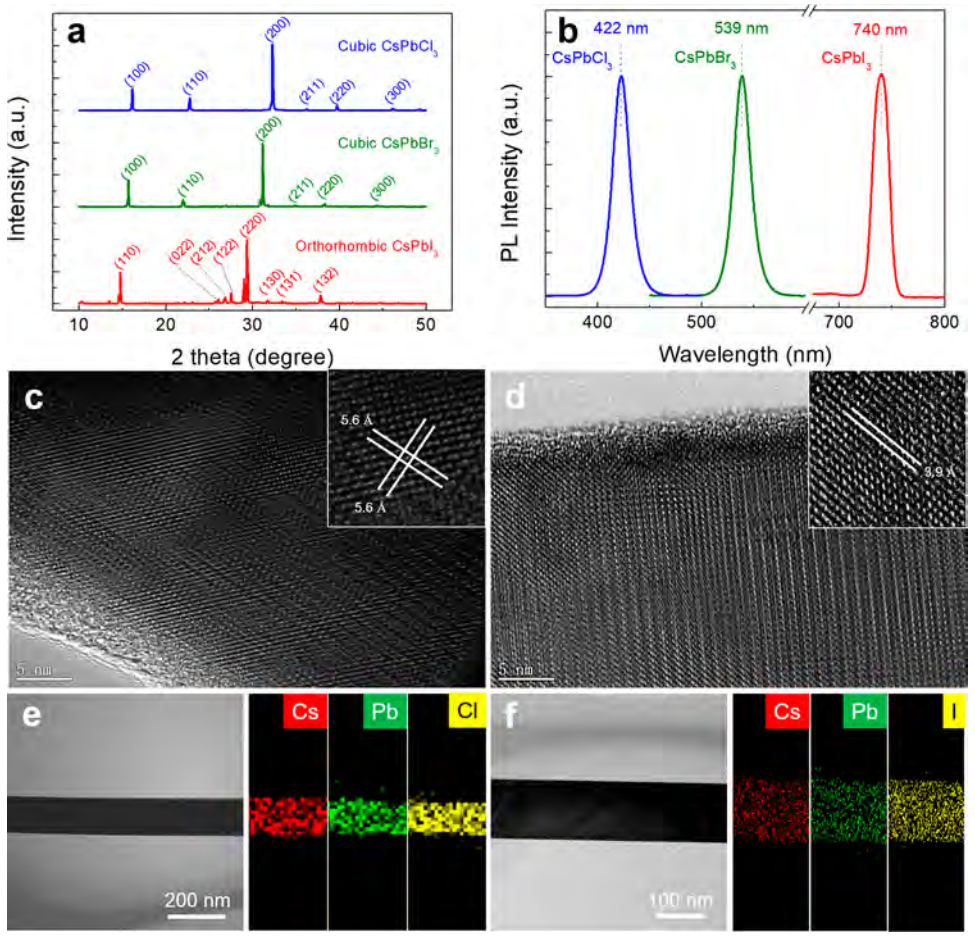

Figure 4. (a) XRD patterns and (b) normalized PL spectra of the VLS-grown $CsPbX_3$ (X = Cl, Br, or I) NWs. HRTEM images and EDS mappings of the VLS-grown (c, e) $CsPbCl_3$ and (d, f) $CsPbI_3$ NW.

Pb content in the catalytic seeds as well as the high melting point of $PbBr_2$ materials. However, we do not exclude the existence of Sn−Pb alloy, $SnBr_2$, and/or LHPs in the same catalytic seeds. In an alloying situation for multicomponent eutectics, the theory of the VLS or vapor−solid−solid (VSS) mechanism is far from clear. Earlier works have reported that the NW growth model significantly depends on the growth pressure, thermal history, catalyst diameter, material flux, *etc.*;[39,40] however, there are still many unexplained phenomena and inconsistencies in the current theory. Additional investigation of the catalytic seed and the liquid−solid interface during VLS growth is needed for the subsequent development of VLS-grown LHPs.

For the VLS NW growth, the most important phenomenon is the selective crystal growth at the liquid−solid interface, which dictates the properties of the NWs obtained.[23,31] This process is somewhat different from the noncatalyzed epitaxial growth of micro/nanowires, in which the crystal growth happens at the vapor−solid interface.[16,17] During the VLS process, the growth is typically determined by the supply of vapor source, which is controlled by the growth temperature and/or growth pressure.[22] Although there has already been a number of studies focusing on the VLS growth kinetics for other nanomaterial systems, the VLS growth kinetics on emerging $CsPbX_3$ NW materials are still very crucial to be investigated for the subsequent material property enhancement. Comparison experiments performed at low pressure (0.5 Torr) demonstrate clearly that both NWs and particles are found to coexist on the growth substrates. With the increasing pressure while holding the other process parameters constant, the density of NWs continues to increase even though there still have a small amount of particles. When the growth pressure is raised to a certain threshold value (1.5 Torr), the high-density vertically aligned NWs can be produced as given in Figure 3a. Thus, the high growth pressure is beneficial to suppress the evaporation of source materials to yield an efficient VLS growth.[16] However, for a relatively high growth pressure (>5 Torr), short NWs with the length of only several micrometers are obtained due to the limited supply of the source vapor.[26]

Besides the process pressure, since the $CsPbX_3$ NW growth occurs *via* crystallization from the liquid catalyst droplets, the NW density is also determined by the density of catalyst droplets located on the substrates. As depicted in the SEM images in Figure 3b, it is obvious that the NW density can be adjusted in a highly controllable way by altering the catalyst density, which again confirms the VLS growth mechanism here. This finding can further advocate the potential of deterministic NW growth and integration *via* simply manipulating the catalyst position. Moreover, the NW nucleation and morphology are as well sensitive to the growth temperature (Figure 3c). The samples grown at the temperatures ranging from 300 to 340 °C indeed show a high yield of NW growth, while the sample grown at the temperature below 300 °C would mainly lead to the growth of particles or plates instead of the NW morphology (Figure S7). The appearance of these particles or plates at the low growth

DOI: 10.1021/acsnano.9b02379
ACS Nano XXXX, XXX, XXX−XXX

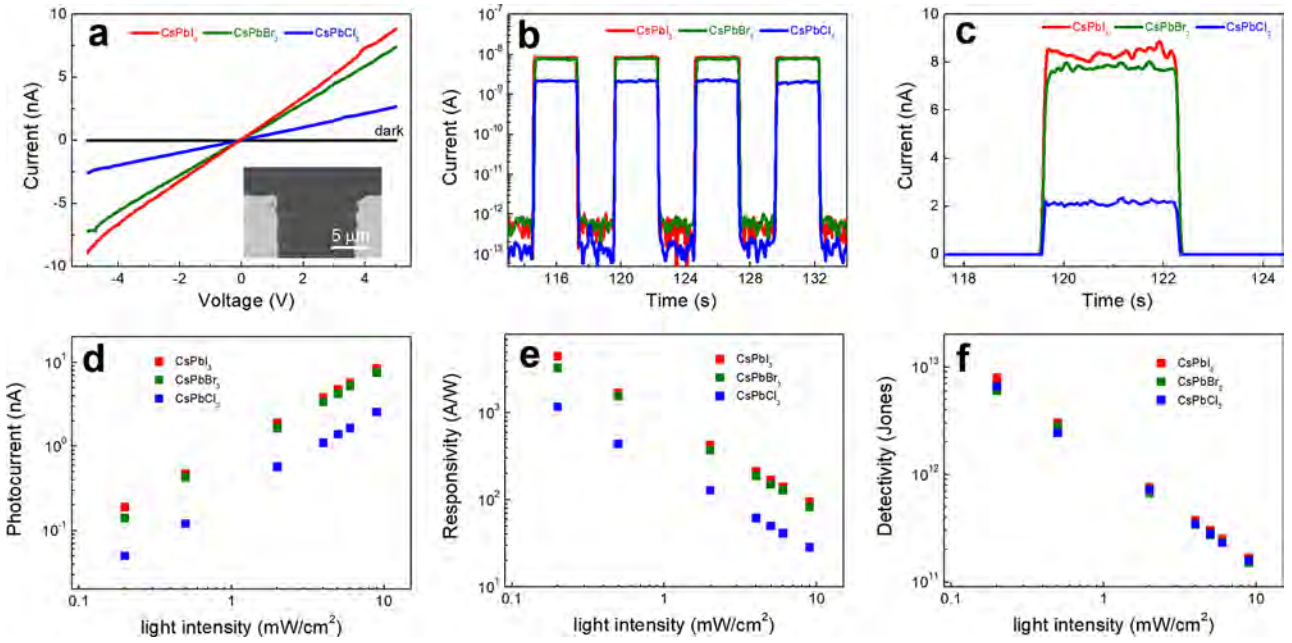

Figure 5. (a) $I-V$ curves of $CsPbX_3$ (X = Cl, Br, or I) NW PDs with and without the light illumination (9 mW/cm^2). Inset shows the SEM image of the as-fabricated NW PD. (b, c) Output current as a function of time under the chopped light illumination (9 mW/cm^2) and a bias voltage of 5 V. (d) Photocurrent, (e) responsivity, and (f) detectivity of $CsPbX_3$ NW PDs as a function of the incident light intensity.

temperature is possible due to the increased precursor decomposition, the lower kinetic barrier for nucleation, and the decrease of adatom diffusion length.[22] The existence of catalytic nanoparticles is also clearly observed at the edge region of these particles and plates, which reveals that the low growth temperature gives the competing VLS and VS growth of nanomaterials at the same time (Figure S7). In contrast, the high growth temperature (350 °C) seems to make the $CsPbBr_3$ NWs hard to nucleate; therefore, only short NWs and small particles are obtained as witnessed in Figure S8. With the optimal conditions, the uniform and vertical $CsPbBr_3$ NW growth can be effectively achieved within a relatively narrow process window (Figure 3c). This narrow window may contribute to the growth challenge here and explain the reason why there has been limited reporting on VLS growth of all-inorganic LHP nanomaterials.

When the growth is optimized, the average NW diameter obtained is around 150 nm that is roughly equal to the diameter of Sn catalysts employed in this work (Figure 3d). This suggests that the diameter of these VLS-grown $CsPbX_3$ NWs can be controllably modified by just altering the catalyst diameter.[38] In the future, the thinner NWs can be grown with the smaller catalyst nanoparticles. In addition, the length of $CsPbX_3$ NWs is found to be directly proportional to the growth time, supporting that the NW growth is a time-dependent process (Figure S9). We also compare the corresponding growth rates of all three kinds of $CsPbX_3$ NWs as compiled in Figure 3e. The $CsPbI_3$ NWs show the higher growth rate (4.17 nm/s) than that of $CsPbBr_3$ NWs (2.78 nm/s) and $CsPbCl_3$ NWs (1.40 nm/s). From the viewpoint of their material properties, this growth rate dependence is highly consistent with the compound melting points of $CsPbX_3$ (476 °C for $CsPbI_3$, 567 °C for $CsPbBr_3$, and 615 °C for $CsPbCl_3$) that are generally indicative of the strength of their atomic interactions (*i.e.*, the bond strength). The bond strength has been proven to play an important role in regulating the interfacial energies and hence critically determines the activation energy barrier height for the NW nucleation (*i.e.*, the growth rate). As a result, increasing the bond strength can widen the VLS growth window but reduce the NW growth rate. Similar observations have also been reported in the metal oxide material systems.[26]

In this case, similar VLS growth processes were also successfully optimized for the synthesis of $CsPbI_3$ and $CsPbCl_3$ NWs. In order to verify their structural quality, X-ray diffraction (XRD) patterns were collected for all $CsPbX_3$ NWs. As shown in Figure 4a, all the sharp diffraction peaks can be indexed to the perovskite phase of $CsPbX_3$, including cubic $CsPbCl_3$ (JCPDS No. 84-0437, $Pm\bar{3}m$ (221), a = 5.605 Å), cubic $CsPbBr_3$ (JCPDS No. 854-0752, $Pm\bar{3}m$ (221), a = 5.83 Å), and orthorhombic $CsPbI_3$ ($Pnam$ (62), a = 8.856 Å, b = 8.576 Å, c = 12.472 Å).[41] Notably, the $CsPbI_3$ NWs are crystallized in the orthorhombic space group at room temperature, adopting a distorted perovskite structure with tilted $\{PbBr_6\}^{4-}$ octahedra. This is slightly different from $CsPbBr_3$ and $CsPbCl_3$ NWs, which adopt a cubic crystal structure. For the $CsPbX_3$ systems, the formation of the perovskite-type structure is greatly dependent on the ionic radius match of Cs, Pb, and halide (Cl, Br, or I) ions. It has been reported that the larger halide ionic radii are often favorable for the formation of the orthorhombic structure, which is attributed to the effective ionic radii that are incompatible with the Goldschmidt tolerance factor (GTF).[41,42] Thus, owing to the large ionic radius of iodine and hence the structural instability, the $CsPbI_3$ NW would tend to crystallize in an orthorhombic structure that is thermally stable at room temperature.

After the successful growth of $CsPbX_3$ NWs, their optical properties were also investigated. As presented in the normalized photoluminescence (PL) spectra in Figure 4b, all $CsPbX_3$ NWs exhibit a single emission band with the spectral peaks shifted from 422 nm (for cubic $CsPbCl_3$), 539 nm (for cubic $CsPbBr_3$), to 740 nm (for orthorhombic $CsPbI_3$), which covers almost the entire visible range. Simply by tuning the halide composition, this wide emission range can designate the practical utilizations of these $CsPbX_3$ NWs for high-performance broadband photonics or optoelectronics.[4,13] Furthermore,

DOI: 10.1021/acsnano.9b02379
ACS Nano XXXX, XXX, XXX−XXX

the crystallinity of VLS-grown $CsPbI_3$ and $CsPbCl_3$ NWs were also evaluated as given in Figure 4c and 4d. The HRTEM images clearly reveal that the $CsPbCl_3$ and $CsPbI_3$ NWs consist of defect-free, single-crystalline cubic and orthorhombic phases, respectively, which is consistent with the XRD results as discussed above. Importantly, these NWs exhibit the smooth surface with amorphous native oxide layers that are the common features of VLS-grown NWs.[24,38] EDS mappings were as well performed on the $CsPbCl_3$ and $CsPbI_3$ NWs, where the uniform elemental distribution and ideal Cs/Pb/X composition ratio of 1:1:3 are obviously observed. All these results explicitly suggest that the VLS growth process can be generally employed for the synthesis of high-quality inorganic LHP nanostructures.

As the VLS NW growth can be optimized especially for the reduced defect concentration (*e.g.*, grain boundaries and structural disorders), these highly crystalline perovskite NWs can allow us to shed light on their intrinsic material properties and hence potential utilizations. In order to demonstrate their optoelectronic applications, single $CsPbX_3$ (X = Cl, Br, or I) NWs were configured into photodetectors (PDs), while corresponding current−voltage (I−V) curves of these NW PDs were measured with and without the light illumination as shown in Figure 5a. It is also noted that laser diodes of 532, 450, and 405 nm were used as the light source for the photodetection measurement of $CsPbI_3$, $CsPbBr_3$, and $CsPbCl_3$ NW PDs, respectively. The SEM image of a typical single $CsPbX_3$ NW PD with a channel length of 10 μm is shown in the Figure 1b inset. The linear relationships of I−V indicate that the contacts between the $CsPbX_3$ NW and Au electrodes are ohmic-like. Specifically, all the PDs with similar NW channel diameters of ∼150 nm give the low dark currents (I_{dark}) of 0.1−1 pA under a bias voltage of 5 V, which is probably originated from the minimized free carrier concentration in high-quality VLS-grown LHP NWs.[43] When illuminated at an intensity of 9 mW/cm^2 under the same bias conditions, the light current (I_{light}) increases by more than 4 orders of magnitude to 8.6 nA, 7.4 nA, and 2.6 nA for $CsPbI_3$, $CsPbBr_3$, and $CsPbCl_3$ NW PDs, respectively. Also, they all exhibit excellent stability and reliability with the on/off switching measurement (Figure 5b and Figure S10). The response times (*i.e.*, rise time and recovery time), defined as the time for the photocurrent ($I_{ph} = I_{light} - I_{dark}$) to vary from 10% to 90% of the peak current, are found to be less than 50 ms (Figure 5c). All these results can indicate the excellent device performance in their corresponding emission band of wavelengths. Simultaneously, the relationship between I_{ph} and incident light intensity is found to obey the power law model of $I_{ph} \propto P^k$, where P is the light intensity and k is an empirical value.[35] Through the nonlinear fitting, we can obtain the k values of 0.95, 0.88, and 0.45 for $CsPbI_3$, $CsPbBr_3$, and $CsPbCl_3$ NW PDs, respectively. The $CsPbI_3$ and $CsPbBr_3$ NWs have similar k values, while that for the $CsPbCl_3$ NW is the smallest, indicating its higher rate of carrier recombination during the photodetection process, agreeing well with its smallest photocurrent among all NW materials as presented in Figure 5a. This sublinear relationship between I_{light} and light intensity resulted from the complex processes of electron−hole generation, trapping, and recombination, which is typically observed for semiconducting materials.[44,45]

On the other hand, responsivity (R) and specific detectivity (D^*) are other important figure-of-merits to quantify the device performance and sensitivity of PDs, which are defined as $R = I_{light}/(PA)$ and $D^* = RA^{1/2}/(2eI_{dark})^{1/2}$, where A is the effective irradiated area on the NW and e is the electronic charge.[46] Here we use the cross-sectional area ($A = L \times d$; L is channel length, d is NW diameter) to estimate the effective irradiated area of the $CsPbX_3$ NW PDs.[47] Figure 5d to 5f depict the values of I_{ph}, R, and D^* at different light intensity. It is clear that both R and D^* increase dramatically with the decreasing light intensity. Under a low light intensity of 0.2 mW/cm^2, the R values of the $CsPbX_3$ NW PDs are as high as 4489, 3306, and 1183 A/W, accordingly, while the corresponding D^* values are up to 7.9×10^{12}, 6.0×10^{12}, and 6.6×10^{12} Jones, for $CsPbI_3$, $CsPbBr_3$, and $CsPbCl_3$, respectively. Table 1 summarizes the key device performance parameters of all current NW PDs. Impressively, these extraordinarily high R and D^* values are better than those for other all-inorganic low-dimensional perovskite PDs reported in the literature (Table S1) and even comparable to those of the inorganic−organic hybrid ones (Table S2), which demonstrate the superior material quality of the VLS-grown single-crystalline $CsPbX_3$ NWs developed in this work.[15,16,18−20] For single-crystalline LHP NW photodetectors, it is commonly accepted that this respectable photodetection performance resulted from the low trap-state density, long carrier diffusion lengths (on the order of 10 μm), and long carrier lifetimes (0.1−1 μs) of NWs, exceeding those of most conventional semiconductors.[5,43]

Table 1. Key Device Performance Parameters of $CsPbX_3$ (X = Cl, Br, or I) NW PDs

	I_{light} (nA)	I_{light}/I_{dark}	R (A/W)	D^* (Jones)	Gain
$CsPbI_3$	8.6	10^4−10^5	4489	7.9×10^{12}	1564
$CsPbBr_3$	7.4	10^4−10^5	3306	6.0×10^{12}	1530
$CsPbCl_3$	2.6	10^4−10^5	1183	6.6×10^{12}	792

Apart from photodetectors, field-effect transistors (FETs) are another important type of technological device. However, since the as-fabricated one-dimensional single-crystalline perovskite micro-/nanowires are usually firmly connected with the substrates (*e.g.*, mica and sapphire)[15−17] or inserted within the engineered templates (*e.g.*, porous alumina membrane),[14,18,19] it is challenging to directly disperse them from the substrates or templates to carry out fabrications of multiterminal devices and importantly to evaluate the fundamental electrical properties of individual NWs. Benefiting from the VLS growth process developed here, bottom-gate top-contact (BGTC) FETs based on single $CsPbX_3$ (X = Cl, Br, or I) NWs could be easily constructed and characterized, allowing us to investigate their charge transport characteristics at room temperature. In order to obtain $CsPbX_3$ perovskite NWs laid down on the substrates for device fabrications, a dry transfer method was used to configure $CsPbX_3$ NWs onto the 270-nm-thick SiO_2/Si substrates (Figure S11). Shadow masking was then utilized to define the source and drain regions, while 5/80 nm thick Ti/Au electrodes were deposited by electron beam evaporation.

Figure 6a displays the typical transfer characteristics (I_{ds}−V_{gs} curves) of different kinds of $CsPbX_3$ NW devices with the gate voltage (V_{gs}) sweeping from 15 to −45 V and the constant source−drain voltage (V_{ds}) at 5 V. All NW FETs show the dominant *p-type* behavior with a slight *n-type* conductance at positive gate voltage, while the current on/off ratios (I_{on}/I_{off}) are found to be 10^2−10^3. As shown in the representative output characteristic (I_{ds}−V_{ds} curves) of $CsPbBr_3$ NW devices in Figure 6b, I_{ds} gradually increases when V_{gs} decreases from 0 V to −20 V with a step of −5 V, which further confirms the dominant *p-type* conducting characteristics of $CsPbX_3$ NWs. This *p-type* behavior could be attributed to two reasons. First, it is possibly due to the

DOI: 10.1021/acsnano.9b02379
ACS Nano XXXX, XXX, XXX−XXX

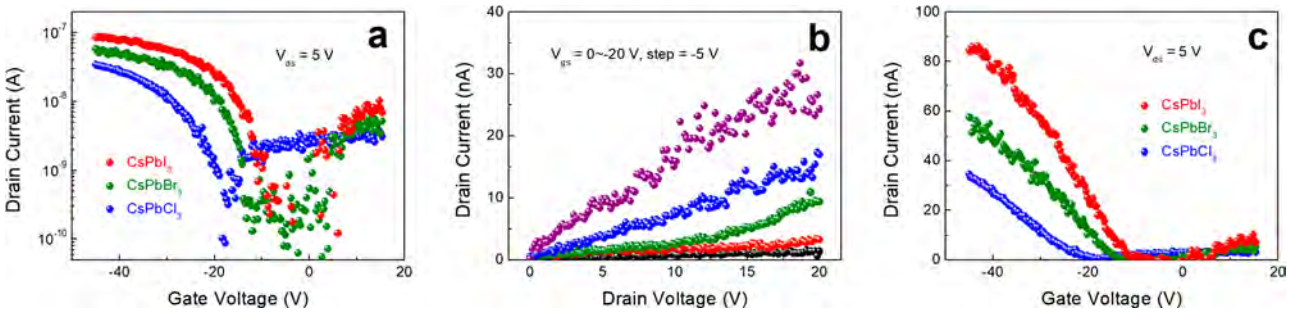

Figure 6. (a) Transfer characteristics of the typical single VLS-grown $CsPbX_3$ (X = Cl, Br, or I) NW FETs using logarithm *y*-coordinate. (b) Output characteristics of the single VLS-grown $CsPbBr_3$ NW FETs. (c) Transfer characteristics of the single $CsPbX_3$ NW FETs using linear *y*-coordinate.

acceptor-like interface trapping states located at the amorphous oxide shells that are observed in HRTEM images (Figure 4c and 4d). Owing to the enhanced surface-to-volume ratio of NWs, the abundant oxide trap states fully deplete electrons in the NWs and hence result in the *p-type* conduction. Similar interface trapping effects have also been reported in GaAs NWs and their devices.[38,48] In the future, p- to n-channel switching behaviors could be achieved in LHP NWs *via* the careful manipulation of interface trapping states. Second, it may be resulted from a self-doping process related to the residual Sn species existing within the NW lattice. To be specific, based on the EDS analysis of $CsPbX_3$ NWs, the NW body is composed of a trace amount of residual Sn species from the catalysts (Figure S3). When these Sn or Sn^{2+} species are oxidized, the resulted Sn^{4+} ions could act as a *p-type* dopant in a process referred as "self-doping"; as a result, they contribute to the *p-type* conducting characteristics of $CsPbX_3$ NWs here.[49] Next, field-effect mobility (μ_{FE}) in the linear regime can be calculated with the analytical equation of $\mu = L^2 g_m/(C_g V_d)$, where L is the channel length, g_m is transconductance (defined as dI_{ds}/dV_{gs}), and C_g is the gate capacitance. The value of C_g is obtained from the finite element analysis software COMSOL tailored for the cylinder on-plane model.[50] With the same device fabrication condition and device geometry, the hole field-effect mobility values are estimated to be 3.05, 2.17, and 1.06 $cm^2/(V\ s)$ for $CsPbI_3$, $CsPbBr_3$, and $CsPbCl_3$ NW FETs, respectively. The Fröhlich coupling mechanism can explain the differences of charge carrier mobility for ionic (polar) semiconductors (*e.g.*, GaAs), which also works well for $CsPbX_3$ here.[34] It has been reported that Fröhlich interactions were found to be enhanced in $APbBr_3$ with respect to $APbI_3$ (for A = MA, FA), which was attributed to the higher ionicity of the Pb−Br bond as compared with the Pb−I bond.[51] Thus, the room-temperature mobility is anticipated to decline across the halide series from $CsPbI_3$ to $CsPbCl_3$, which is possibly due to the increasing ionicity of the Pb−X bond. This Fröhlich coupling may as well explain the smallest photocurrent value obtained for $CsPbCl_3$ PDs as discussed above. It is also worth noting that the reported hole mobility values here are even more superior than many other semiconductors, such as metal oxides and (pseudo) halides used for p-channel FETs.[52] These high field-effect mobility values measured at room temperature could be attributed to the defect-free single-crystalline nature of our VLS-grown all-inorganic perovskite NWs.

Furthermore, the device threshold voltage (V_{th}) can be extracted from the slope and *x*-axis intercept of I_{ds}-V_{gs} curves (Figure 6c),[53] in which the V_{th} values are found to be −10.9, −13.9, and −21.5 V for the FETs based on $CsPbI_3$, $CsPbBr_3$, and $CsPbCl_3$ NW, respectively. These different V_{th} values are usually associated with the different amounts of carrier concentration (n). This concentration can be estimated by the analytical expression of $n = 4C_g(V_{gs} - V_{th})/qd^2L$, where d is the NW radius and L is the channel length.[54] At V_g = −45 V, the average values of n are determined to be 3.62×10^{18} cm^{-3} for $CsPbI_3$, 3.29×10^{18} cm^{-3} for $CsPbBr_3$, and 2.49×10^{18} cm^{-3} for $CsPbCl_3$. The difference of carrier concentration can as well be explained by the Fröhlich coupling existed in the $CsPbX_3$ system.[34,51] Meanwhile, the reduced n and μ_{FE} values, across the halide series from $CsPbI_3$ to $CsPbCl_3$, also lead to the slight decrease of on-current (I_{on}), as shown in Figure 6c and Table 2. Although our single-crystalline perovskite NW FETs show impressive device characteristics, there is definitely great potential to further enhance the device performance through various strategies, including the perovskite material design, device passivation, and device miniaturization.[34,43]

Table 2. Key Device Performance Parameters of $CsPbX_3$ (X = Cl, Br, or I) NW FETs

	Mobility ($cm^2/(V\ s)$)	I_{on} (nA)	I_{on}/I_{off}	V_{th} (V)	n (cm^{-3})
$CsPbI_3$	3.05	85	$>10^3$	−10.9	3.62×10^{18}
$CsPbBr_3$	2.17	57	$>10^3$	−13.9	3.29×10^{18}
$CsPbCl_3$	1.06	35	$>10^2$	−21.5	2.49×10^{18}

CONCLUSIONS

In this work, we developed a direct VLS method to obtain $CsPbX_3$ (X = Cl, Br, and I) NWs by using Sn catalysts. The VLS mechanism allows us to synthesize defect-free single-crystalline $CsPbX_3$ NWs with precise control over the microstructural morphology, nanowire density, and chemical composition. The structural characterization shows that NWs all existed in the stable cubic (for $CsPbBr_3$ and $CsPbCl_3$) or orthorhombic (for $CsPbI_3$) phase at room temperature. In order to demonstrate their optoelectronic applications, single $CsPbX_3$ NWs are configured as photodetectors with respectable photodetection performance (responsivity exceeding 4489 A/W and detectivity exceeding 7.9×10^{12} Jones) toward the visible light regime. Meanwhile, we also demonstrate field-effect transistors based on an individual $CsPbX_3$ NW, which exhibits superior hole field-effect mobility of 3.05 $cm^2/(V\ s)$ measured at room temperature. Overall, these VLS-grown perovskite NWs can provide versatile platforms for evaluating the fundamental properties and exploring the potential applications of one-dimensional perovskite nanostructures.

DOI: 10.1021/acsnano.9b02379
ACS Nano XXXX, XXX, XXX−XXX

METHODS

Material Synthesis. All chemicals were purchased from Sigma-Aldrich and used without further purification. The growth substrate was prepared by drop-casting an aqueous Sn nanoparticle (150 nm particle size, ⩾99%, Aldrich) suspension onto a *p-type* Si substrate with a 270 nm thick thermal oxide layer. The source powder of $CsPbX_3$ was prepared by mixing CsX and PbX_2 with a molar ratio of 1:2 and then annealed (at 420 °C for $CsPbI_3$, 430 °C for $CsPbBr_3$, 460 °C for $CsPbCl_3$) for 30 min at atmosphere before being placed into the tube furnace. The VLS growth of the $CsPbX_3$ (X = Cl, Br, or I) NWs was carried out in a two-zone chemical vapor deposition (CVD) system equipped with a quartz tube (1-in. inner diameter). The $CsPbX_3$ source powder was placed inside the high-temperature heating zone with temperature settings of 430 °C ($CsPbI_3$), 440 °C ($CsPbBr_3$), and 470 °C ($CsPbCl_3$). The substrates with Sn nanoparticles were placed inside the low-temperature heating zone with temperature settings of 290 °C ($CsPbI_3$), 310 °C ($CsPbBr_3$), and 330 °C ($CsPbCl_3$). The reactor was evacuated to a base pressure of ~0.15 mTorr, and then argon (80 Sccm) and hydrogen (15 Sccm) were flowed through the reactor. The growth pressure was set to 0.3−5 Torr as required during the entire growth process. To initiate the VLS growth process of $CsPbX_3$ NWs, source powder was vaporized at an elevated temperature and carried to the low-temperature zone by mixed argon/hydrogen gas. After the preset growth duration (60−300 min), the reaction was terminated, and immediately the furnace lid was opened to cool down.

Material Characterization. Surface morphologies of the NWs were examined using a scanning electron microscope (SEM, Philips XL30) and a transmission electron microscope (TEM, Philips CM-20). Crystal structures were determined by collecting the XRD pattern on a Philips powder diffractometer and imaging with a high-resolution TEM (HRTEM, JEOL 2100F). The PL spectra were acquired by iHR320 photoluminescence spectroscopy with excitation wavelengths of 635 nm for $CsPbI_3$, 425 nm for $CsPbBr_3$, and 365 nm for $CsPbCl_3$. Elemental mappings and line scan were performed using an energy dispersive X-ray (EDS) detector attached to a JEOL 2100F.

Device Fabrication and Characterization. In order to obtain $CsPbX_3$ NWs laid down on the substrates for subsequent device studies, a dry transfer method was used to separate the NWs from the growth substrates. Afterward, shadow masking was utilized to define the source and drain regions, and 5/80 nm thick Ti/Au film electrodes were deposited by electron beam evaporation. The channel lengths were 10 μm for all the devices performed in this study. Device characterizations were performed in ambient atmosphere with an Agilent 4155C semiconductor analyzer and a standard electrical probe station. In this work, laser diodes of 532, 450, and 405 nm were used as the light source for the photodetection measurement of $CsPbI_3$, $CsPbBr_3$, and $CsPbCl_3$ NWs, respectively. The power of the incident irradiation was measured using a power meter (PM400, Thorlabs).

ASSOCIATED CONTENT

Supporting Information

The Supporting Information is available free of charge on the ACS Publications website at DOI: 10.1021/acsnano.9b02379.

Optical images, EDS analysis, XRD patterns and normalized PL spectra of $CsPbBr_3$ NWs; TEM images of VLS-grown $CsPbI_3$ and $CsPbCl_3$ NWs with distinctive catalytic tips; SEM images of $CsPbBr_3$ nanostructures grown at different temperature and with different growth time; On/off switching measurement of $CsPbI_3$, $CsPbBr_3$, and $CsPbCl_3$ NW PDs; Performance summary of photodetectors based on low-dimensional all-inorganic LHPs and inorganic−organic hybrid LHPs (PDF)

AUTHOR INFORMATION

Corresponding Author

*E-mail: johnnyho@cityu.edu.hk.

ORCID

Renjie Wei: 0000-0002-0459-7196
Xiuming Bu: 0000-0002-2372-2271
Johnny C. Ho: 0000-0003-3000-8794

Notes

The authors declare no competing financial interest.

ACKNOWLEDGMENTS

We acknowledge the General Research Fund of the Research Grants Council of Hong Kong SAR, China (CityU 11204618), the National Natural Science Foundation of China (Grant 51672229), the Science Technology and Innovation Committee of Shenzhen Municipality (Grant JCYJ20170818095520778), and a grant from the Shenzhen Research Institute, City University of Hong Kong.

REFERENCES

(1) Chen, Q.; Wu, J.; Ou, X.; Huang, B.; Almutlaq, J.; Zhumekenov, A. A.; Guan, X.; Han, S.; Liang, L.; Yi, Z.; Li, J.; Xie, X.; Wang, Y.; Li, Y.; Fan, D.; Teh, D. B. L.; All, A. H.; Mohammed, O. F.; Bakr, O. M.; Wu, T.; Bettinelli, M.; Yang, H.; Huang, W.; Liu, X. All-Inorganic Perovskite Nanocrystal Scintillators. *Nature* **2018**, *561*, 88−93.

(2) Lin, K.; Xing, J.; Quan, L. N.; de Arquer, F. P. G.; Gong, X.; Lu, J.; Xie, L.; Zhao, W.; Zhang, D.; Yan, C.; Li, W.; Liu, X.; Lu, Y.; Kirman, J.; Sargent, E. H.; Xiong, Q.; Wei, Z. Perovskite Light-Emitting Diodes with External Quantum Efficiency Exceeding 20 Per Cent. *Nature* **2018**, *562*, 245−248.

(3) Raino, G.; Becker, M. A.; Bodnarchuk, M. I.; Mahrt, R. F.; Kovalenko, M. V.; Stoferle, T. Superfluorescence from Lead Halide Perovskite Quantum Dot Superlattices. *Nature* **2018**, *563*, 671−675.

(4) Fu, Y.; Zhu, H.; Stoumpos, C. C.; Ding, Q.; Wang, J.; Kanatzidis, M. G.; Zhu, X.; Jin, S. Broad Wavelength Tunable Robust Lasing from Single-Crystal Nanowires of Cesium Lead Halide Perovskites ($CsPbX_3$, X = Cl, Br, I). *ACS Nano* **2016**, *10*, 7963−7972.

(5) Zhu, H.; Fu, Y.; Meng, F.; Wu, X.; Gong, Z.; Ding, Q.; Gustafsson, M. V.; Trinh, M. T.; Jin, S.; Zhu, X. Y. Lead Halide Perovskite Nanowire Lasers with Low Lasing Thresholds and High Quality Factors. *Nat. Mater.* **2015**, *14*, 636−642.

(6) Hu, X.; Zhou, H.; Jiang, Z.; Wang, X.; Yuan, S.; Lan, J.; Fu, Y.; Zhang, X.; Zheng, W.; Wang, X.; Zhu, X.; Liao, L.; Xu, G.; Jin, S.; Pan, A. Direct Vapor Growth of Perovskite $CsPbBr_3$ Nanoplate Electroluminescence Devices. *ACS Nano* **2017**, *11*, 9869−9876.

(7) Hu, X.; Wang, X.; Fan, P.; Li, Y.; Zhang, X.; Liu, Q.; Zheng, W.; Xu, G.; Wang, X.; Zhu, X.; Pan, A. Visualizing Carrier Transport in Metal Halide Perovskite Nanoplates *via* Electric Field Modulated Photoluminescence Imaging. *Nano Lett.* **2018**, *18*, 3024−3031.

(8) Feng, J.; Gong, C.; Gao, H.; Wen, W.; Gong, Y.; Jiang, X.; Zhang, B.; Wu, Y.; Wu, Y.; Fu, H.; Jiang, L.; Zhang, X. Single-Crystalline Layered Metal-Halide Perovskite Nanowires for Ultrasensitive Photodetectors. *Nature Electronics* **2018**, *1*, 404−410.

(9) Lei, T.; Lai, M.; Kong, Q.; Lu, D.; Lee, W.; Dou, L.; Wu, V.; Yu, Y.; Yang, P. Electrical and Optical Tunability in All-Inorganic Halide Perovskite Alloy Nanowires. *Nano Lett.* **2018**, *18*, 3538−3542.

(10) Zhang, X.; Chen, S.; Wang, X.; Pan, A. Controlled Synthesis and Photonics Applications of Metal Halide Perovskite Nanowires. *Small Methods* **2019**, *3*, 1800294.

(11) Quintero-Bermudez, R.; Gold-Parker, A.; Proppe, A. H.; Munir, R.; Yang, Z.; Kelley, S. O.; Amassian, A.; Toney, M. F.; Sargent, E. H. Compositional and Orientational Control in Metal Halide Perovskites of Reduced Dimensionality. *Nat. Mater.* **2018**, *17*, 900−907.

(12) Xing, J.; Liu, X. F.; Zhang, Q.; Ha, S. T.; Yuan, Y. W.; Shen, C.; Sum, T. C.; Xiong, Q. Vapor Phase Synthesis of Organometal Halide Perovskite Nanowires for Tunable Room-Temperature Nanolasers. *Nano Lett.* **2015**, *15*, 4571−4577.

(13) Park, K.; Lee, J. W.; Kim, J. D.; Han, N. S.; Jang, D. M.; Jeong, S.; Park, J.; Song, J. K. Light-Matter Interactions in Cesium Lead Halide Perovskite Nanowire Lasers. *J. Phys. Chem. Lett.* **2016**, *7*, 3703−3710.

DOI: 10.1021/acsnano.9b02379
ACS Nano XXXX, XXX, XXX−XXX

(14) Gu, L.; Tavakoli, M. M.; Zhang, D.; Zhang, Q.; Waleed, A.; Xiao, Y.; Tsui, K. H.; Lin, Y.; Liao, L.; Wang, J.; Fan, Z. 3D Arrays of 1024-Pixel Image Sensors Based on Lead Halide Perovskite Nanowires. *Adv. Mater.* **2016**, *28*, 9713−9721.
(15) Chen, J.; Fu, Y.; Samad, L.; Dang, L.; Zhao, Y.; Shen, S.; Guo, L.; Jin, S. Vapor-Phase Epitaxial Growth of Aligned Nanowire Networks of Cesium Lead Halide Perovskites ($CsPbX_3$, X = Cl, Br, I). *Nano Lett.* **2017**, *17*, 460−466.
(16) Shoaib, M.; Zhang, X.; Wang, X.; Zhou, H.; Xu, T.; Wang, X.; Hu, X.; Liu, H.; Fan, X.; Zheng, W.; Yang, T.; Yang, S.; Zhang, Q.; Zhu, X.; Sun, L.; Pan, A. Directional Growth of Ultralong $CsPbBr_3$ Perovskite Nanowires for High-Performance Photodetectors. *J. Am. Chem. Soc.* **2017**, *139*, 15592−15595.
(17) Wang, X.; Shoaib, M.; Wang, X.; Zhang, X.; He, M.; Luo, Z.; Zheng, W.; Li, H.; Yang, T.; Zhu, X.; Ma, L.; Pan, A. High-Quality In-Plane Aligned $CsPbX_3$ Perovskite Nanowire Lasers with Composition-Dependent Strong Exciton-Photon Coupling. *ACS Nano* **2018**, *12*, 6170−6178.
(18) Waleed, A.; Tavakoli, M. M.; Gu, L.; Hussain, S.; Zhang, D.; Poddar, S.; Wang, Z.; Zhang, R.; Fan, Z. All Inorganic Cesium Lead Iodide Perovskite Nanowires with Stabilized Cubic Phase at Room Temperature and Nanowire Array-Based Photodetectors. *Nano Lett.* **2017**, *17*, 4951−4957.
(19) Waleed, A.; Tavakoli, M. M.; Gu, L.; Wang, Z.; Zhang, D.; Manikandan, A.; Zhang, Q.; Zhang, R.; Chueh, Y. L.; Fan, Z. Lead-Free Perovskite Nanowire Array Photodetectors with Drastically Improved Stability in Nanoengineering Templates. *Nano Lett.* **2017**, *17*, 523−530.
(20) Oksenberg, E.; Sanders, E.; Popovitz-Biro, R.; Houben, L.; Joselevich, E. Surface-Guided $CsPbBr_3$ Perovskite Nanowires on Flat and Faceted Sapphire with Size-Dependent Photoluminescence and Fast Photoconductive Response. *Nano Lett.* **2018**, *18*, 424−433.
(21) Ek, M.; Filler, M. A. Atomic-Scale Choreography of Vapor-Liquid-Solid Nanowire Growth. *Acc. Chem. Res.* **2018**, *51*, 118−126.
(22) Zhu, Z.; Suzuki, M.; Nagashima, K.; Yoshida, H.; Kanai, M.; Meng, G.; Anzai, H.; Zhuge, F.; He, Y.; Boudot, M.; Takeda, S.; Yanagida, T. Rational Concept for Reducing Growth Temperature in Vapor-Liquid-Solid Process of Metal Oxide Nanowires. *Nano Lett.* **2016**, *16*, 7495−7502.
(23) Tian, B.; Xie, P.; Kempa, T. J.; Bell, D. C.; Lieber, C. M. Single-Crystalline Kinked Semiconductor Nanowire Superstructures. *Nat. Nanotechnol.* **2009**, *4*, 824−829.
(24) Yang, Z. X.; Liu, L.; Yip, S.; Li, D.; Shen, L.; Zhou, Z.; Han, N.; Hung, T. F.; Pun, E. Y.; Wu, X.; Song, A.; Ho, J. C. Complementary Metal Oxide Semiconductor-Compatible, High-Mobility, 111-Oriented GaSb Nanowires Enabled by Vapor-Solid-Solid Chemical Vapor Deposition. *ACS Nano* **2017**, *11*, 4237−4246.
(25) Sun, J.; Yin, Y.; Han, M.; Yang, Z. X.; Lan, C.; Liu, L.; Wang, Y.; Han, N.; Shen, L.; Wu, X.; Ho, J. C. Nonpolar-Oriented Wurtzite InP Nanowires with Electron Mobility Approaching the Theoretical Limit. *ACS Nano* **2018**, *12*, 10410−10418.
(26) Klamchuen, A.; Suzuki, M.; Nagashima, K.; Yoshida, H.; Kanai, M.; Zhuge, F.; He, Y.; Meng, G.; Kai, S.; Takeda, S.; Kawai, T.; Yanagida, T. Rational Concept for Designing Vapor-Liquid-Solid Growth of Single Crystalline Metal Oxide Nanowires. *Nano Lett.* **2015**, *15*, 6406−6412.
(27) Guo, P.; Xu, J.; Gong, K.; Shen, X.; Lu, Y.; Qiu, Y.; Xu, J.; Zou, Z.; Wang, C.; Yan, H.; Luo, Y.; Pan, A.; Zhang, H.; Ho, J. C.; Yu, K. M. On-Nanowire Axial Heterojunction Design for High-Performance Photodetectors. *ACS Nano* **2016**, *10*, 8474−8481.
(28) del Alamo, J. A. Nanometre-Scale Electronics with III-V Compound Semiconductors. *Nature* **2011**, *479*, 317−323.
(29) Goktas, N. I.; Wilson, P.; Ghukasyan, A.; Wagner, D.; McNamee, S.; LaPierre, R. R. Nanowires for Energy: A Review. *Appl. Phys. Rev.* **2018**, *5*, No. 041305.
(30) Meyers, J. K.; Kim, S.; Hill, D. J.; Cating, E. E. M.; Williams, L. J.; Kumbhar, A. S.; McBride, J. R.; Papanikolas, J. M.; Cahoon, J. F. Self-Catalyzed Vapor-Liquid-Solid Growth of Lead Halide Nanowires and Conversion to Hybrid Perovskites. *Nano Lett.* **2017**, *17*, 7561−7568.
(31) Jacobsson, D.; Panciera, F.; Tersoff, J.; Reuter, M. C.; Lehmann, S.; Hofmann, S.; Dick, K. A.; Ross, F. M. Interface Dynamics and Crystal Phase Switching in GaAs Nanowires. *Nature* **2016**, *531*, 317−322.
(32) Zhang, X.; Li, L.; Sun, Z.; Luo, J. Rational Chemical Doping of Metal Halide Perovskites. *Chem. Soc. Rev.* **2019**, *48*, 517−539.
(33) Swarnkar, A.; Ravi, V. K.; Nag, A. Beyond Colloidal Cesium Lead Halide Perovskite Nanocrystals: Analogous Metal Halides and Doping. *ACS Energy Lett.* **2017**, *2*, 1089−1098.
(34) Herz, L. M. Charge-Carrier Mobilities in Metal Halide Perovskites: Fundamental Mechanisms and Limits. *ACS Energy Lett.* **2017**, *2*, 1539−1548.
(35) Lan, C.; Dong, R.; Zhou, Z.; Shu, L.; Li, D.; Yip, S.; Ho, J. C. Large-Scale Synthesis of Freestanding Layer-Structured PbI_2 and $MAPbI_3$ Nanosheets for High-Performance Photodetection. *Adv. Mater.* **2017**, *29*, 1702759.
(36) Niu, G.; Yu, H.; Li, J.; Wang, D.; Wang, L. Controlled Orientation of Perovskite Films through Mixed Cations toward High Performance Perovskite Solar Cells. *Nano Energy* **2016**, *27*, 87−94.
(37) Zhou, H.; Yuan, S.; Wang, X.; Xu, T.; Wang, X.; Li, H.; Zheng, W.; Fan, P.; Li, Y.; Sun, L.; Pan, A. Vapor Growth and Tunable Lasing of Band Gap Engineered Cesium Lead Halide Perovskite Micro/Nanorods with Triangular Cross Section. *ACS Nano* **2017**, *11*, 1189−1195.
(38) Han, N.; Hou, J. J.; Wang, F.; Yip, S.; Yen, Y. T.; Yang, Z. X.; Dong, G.; Hung, T.; Chueh, Y. L.; Ho, J. C. GaAs Nanowires: From Manipulation of Defect Formation to Controllable Electronic Transport Properties. *ACS Nano* **2013**, *7*, 9138−9146.
(39) Persson, A. I.; Larsson, M. W.; Stenstrom, S.; Ohlsson, B. J.; Samuelson, L.; Wallenberg, L. R. Solid-Phase Diffusion Mechanism for GaAs Nanowire Growth. *Nat. Mater.* **2004**, *3*, 677−681.
(40) Kodambaka, S.; Tersoff, J.; Reuter, M. C.; Ross, F. M. Germanium Nanowire Growth Below the Eutectic Temperature. *Science* **2007**, *316*, 729−732.
(41) Sutton, R. J.; Filip, M. R.; Haghighirad, A. A.; Sakai, N.; Wenger, B.; Giustino, F.; Snaith, H. J. Cubic or Orthorhombic? Revealing the Crystal Structure of Metastable Black-Phase $CsPbI_3$ by Theory and Experiment. *ACS Energy Lett.* **2018**, *3*, 1787−1794.
(42) Marronnier, A.; Roma, G.; Boyer-Richard, S.; Pedesseau, L.; Jancu, J. M.; Bonnassieux, Y.; Katan, C.; Stoumpos, C. C.; Kanatzidis, M. G.; Even, J. Anharmonicity and Disorder in the Black Phases of Cesium Lead Iodide Used for Stable Inorganic Perovskite Solar Cells. *ACS Nano* **2018**, *12*, 3477−3486.
(43) Fu, Y.; Zhu, H.; Chen, J.; Hautzinger, M. P.; Zhu, X. Y.; Jin, S. Metal Halide Perovskite Nanostructures for Optoelectronic Applications and the Study of Physical Properties. *Nat. Rev. Mater.* **2019**, *4*, 169−188.
(44) Lan, C.; Zhou, Z.; Zhou, Z.; Li, C.; Shu, L.; Shen, L.; Li, D.; Dong, R.; Yip, S.; Ho, J. C. Wafer-Scale Synthesis of Monolayer WS_2 for High-Performance Flexible Photodetectors by Enhanced Chemical Vapor Deposition. *Nano Res.* **2018**, *11*, 3371−3384.
(45) Dong, R.; Lan, C.; Xu, X.; Liang, X.; Hu, X.; Li, D.; Zhou, Z.; Shu, L.; Yip, S.; Li, C.; Tsang, S. W.; Ho, J. C. Novel Series of Quasi-2D Ruddlesden-Popper Perovskites Based on Short-Chained Spacer Cation for Enhanced Photodetection. *ACS Appl. Mater. Interfaces* **2018**, *10*, 19019−19026.
(46) Liu, X.; Gu, L.; Zhang, Q.; Wu, J.; Long, Y.; Fan, Z. All-Printable Band-Edge Modulated ZnO Nanowire Photodetectors with Ultra-High Detectivity. *Nat. Commun.* **2014**, *5*, 4007.
(47) Zheng, D.; Fang, H.; Long, M.; Wu, F.; Wang, P.; Gong, F.; Wu, X.; Ho, J. C.; Liao, L.; Hu, W. High-Performance Near-Infrared Photodetectors Based on *p-type* SnX (X = S, Se) Nanowires Grown *via* Chemical Vapor Deposition. *ACS Nano* **2018**, *12*, 7239−7245.
(48) Han, N.; Wang, F.; Hou, J. J.; Xiu, F.; Yip, S.; Hui, A. T.; Hung, T.; Ho, J. C. Controllable P−N Switching Behaviors of GaAs Nanowires *via* an Interface Effect. *ACS Nano* **2012**, *6*, 4428−4433.
(49) Noel, N. K.; Stranks, S. D.; Abate, A.; Wehrenfennig, C.; Guarnera, S.; Haghighirad, A.-A.; Sadhanala, A.; Eperon, G. E.; Pathak, S. K.; Johnston, M. B.; Petrozza, A.; Herz, L. M.; Snaith, H. J. Lead-Free

DOI: 10.1021/acsnano.9b02379
ACS Nano XXXX, XXX, XXX−XXX

Organic−Inorganic Tin Halide Perovskites for Photovoltaic Applications. *Energy Environ. Sci.* **2014**, *7*, 3061−3068.
(50) Yang, Z. X.; Wang, F.; Han, N.; Lin, H.; Cheung, H. Y.; Fang, M.; Yip, S.; Hung, T.; Wong, C. Y.; Ho, J. C. Crystalline GaSb Nanowires Synthesized on Amorphous Substrates: From the Formation Mechanism to P-Channel Transistor Applications. *ACS Appl. Mater. Interfaces* **2013**, *5*, 10946−10952.
(51) Wright, A. D.; Verdi, C.; Milot, R. L.; Eperon, G. E.; Perez-Osorio, M. A.; Snaith, H. J.; Giustino, F.; Johnston, M. B.; Herz, L. M. Electron-Phonon Coupling in Hybrid Lead Halide Perovskites. *Nat. Commun.* **2016**, *7*, 11755.
(52) Liu, A.; Zhu, H.; Noh, Y.-Y. Solution-Processed Inorganic P-Channel Transistors: Recent Advances and Perspectives. *Mater. Sci. Eng., R* **2019**, *135*, 85−100.
(53) Uemura, T.; Rolin, C.; Ke, T. H.; Fesenko, P.; Genoe, J.; Heremans, P.; Takeya, J. On the Extraction of Charge Carrier Mobility in High-Mobility Organic Transistors. *Adv. Mater.* **2016**, *28*, 151−155.
(54) Zou, X.; Liu, X.; Wang, C.; Jiang, Y.; Wang, Y.; Xiao, X.; Ho, J. C.; Li, J.; Jiang, C.; Xiong, Q.; Liao, L. Controllable Electrical Properties of Metal-Doped In_2O_3 Nanowires for High-Performance Enhancement-Mode Transistors. *ACS Nano* **2013**, *7*, 804−810.

DOI: 10.1021/acsnano.9b02379
ACS Nano XXXX, XXX, XXX−XXX